Chapter 5

Magnetization reversal processes in EB systems investigated via Polarized Neutron Reflectometry (PNR)

5.1 Introduction

It is of technological importance and of scientific interest to be able to understand and to investigate magnetization reversal processes in thin magnetic layer systems. Therefore several research groups have focused on studying the reversal processes in thin film EB-systems. EB can be expected to reveal its unidirectional character during the magnetization reversals. This was confirmed by a number of EB systems, where different reversal processes were observed on opposite sides of the hysteresis loop. This asymmetric behavior can be identified readily by the shape of the hysteretic magnetization curve in at least some systems [CL82, KKH$^+$98, JML$^+$99, XW00, GR00a].

Magnetization curves belong to the fundamental features characterizing the macroscopic properties of ferromagnetic materials. The specific type of reversal is determined by various subtle contributions such as exchange interaction or magnetic anisotropy. Magnetization can be reversed either by rotation or by domain wall motion. For single thin layers, nucleation and domain wall motion is the dominant mechanism because it is energetically more favorable. For granular soft magnetic materials, the relevant mechanism can strongly depend

on the direction of the magneto-crystalline anisotropy [MMT61] or material composition [KUEV98]. For double layers such as AFM/FM systems, reversal may drastically change due to the coupling at the interface. Recent investigations have shown that depending on the particular system both domain wall motion and rotation can be preferred [Nik98, Nik00, FYL$^+$00, PPLdM$^+$00, LFY$^+$01, BK71, CYC$^+$00]. In this work, a PNR study is presented, exploring the magnetization reversal processes in a $[Co/CoO/Au]_{20}$ multilayer. In order to investigate the magnetization reversal processes, the specular and off-specular scattered neutrons are detected at different characteristic magnetic fields from the multilayer in the biased state. This study further elucidates the mechanisms characteristic of the magnetization reversal processes in an EB multilayer consisting of granular Co/CoO bilayers.

5.2 Polarized Neutron Reflectometry

Polarized Neutron Reflection (PNR) has proved to be a suitable technique for the investigation of magnetic and structural properties of thin magnetic films. The small absorption cross section for neutrons in matter leads to sufficiently large penetration depths for the investigation even of multilayer systems [Zab94a], [Bla94]. In contrast to the measurements with neutrons, other measurement techniques, which use electrons for the material analysis, such as e.g. LEED and AES, are sensitive mainly to structural and chemical properties in the area close to the surface. In comparison with X-ray scattering, which is sensitive to the electron density distribution, neutrons interact with the nuclei and the magnetic moments of matter. In addition, neutron reflectometers are generally operated at larger neutron wavelengths which leads to a larger lateral coherence length for the neutron beam (between 10 and 300 μm). This provides the possibility of sampling magnetic domains even when the domain size becomes large.

Besides conventional magnetometry such as SQUID, Polarized Neutron Reflectometry (PNR) is well suited to study reversal processes. Measuring the non-spin-flip (NSF) reflectivities of up-neutrons (R^{++}) and down-neutrons (R^{--}), PNR can be used as a classical magnetometer. The first and second superscript denote the spin orientation of the incoming and scattered neutrons, i.e. before and after interacting with the sample magnetization. By measuring the spin-flip (SF) intensities R^{+-} and R^{-+}, one can additionally exploit the unique property of neutrons, that their spin is flipped if the magnetization in the sample has an in-plane component perpendicular to the initial spin polarization axis. To further elucidate the mechanisms responsible for asymmetric magnetization curves, PNR provides therefore the possibility to measure not

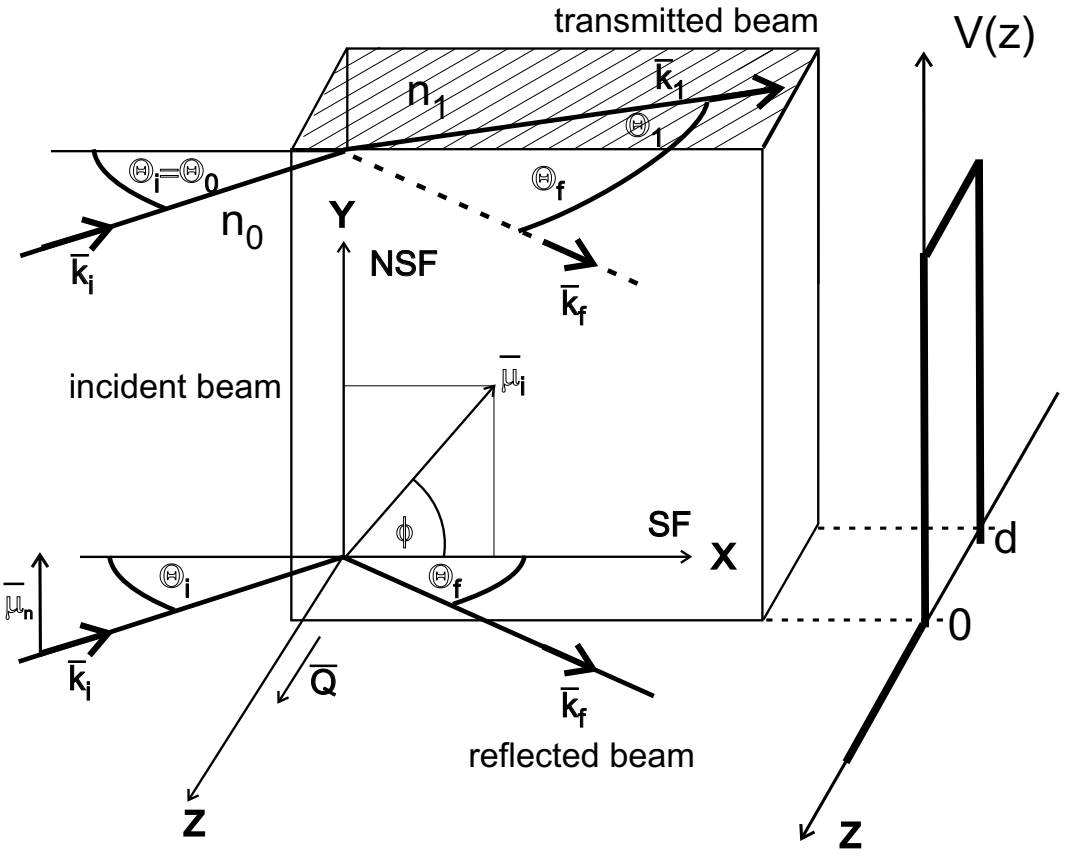

Figure 5.1: Scattering geometry for spin polarized neutrons in a PNR experiment using a continuous and monochromatic neutron beam.

only the in-plane magnetization parallel but also perpendicular to the external field. For a detailed description of the method see Ref. [Zab94a] and references therein.

The following section will describe the interaction of a neutron beam with matter when penetrating the surface of magnetic (multi)layers at low angles.

5.2.1 Scattering theory

The scattering geometry in a typical reflectometry experiment is given in Fig. 5.1. The neutron radiation is characterized by the wave vector $\vec{k}_i$ and its de Broglie wavelength $\lambda = \frac{2\pi}{|\vec{k}_i|}$. The neutron beam hits the sample at an angle Θ_i and is scattered at an angle Θ_f. The scattering vector $\vec{Q}$, which describes

the momentum transfer, is defined as follows

$$|\vec{Q}| = |\vec{k_f} - \vec{k_i}|. \tag{5.1}$$

For the case of specular reflection, i.e. Θ_f=Θ_i=Θ, Eq. 5.1 simplifies to the well known equation

$$|\vec{Q}| = \frac{4\pi}{\lambda} \sin\Theta. \tag{5.2}$$

In the following sections only specular scattering will be considered. Off-specular scattering, i.e. $\Theta_f \neq \Theta_i$, which might occur due to (magnetic or chemical) in-plane structures will be treated only in the next to the last section of this chapter. In the present geometry the scattering vector $\vec{Q}$ is directed perpendicular to the sample surface. Performing a reflectometry experiment, the specular reflected intensity is registered as a function of the momentum transfer $\vec{Q}$.

Following Eq. 5.1 there are two possibilities to perform a reflectometry experiment:

- The angle Θ_i of the incoming beam can be varied if monochromatic radiation is used. This method is applied in the case of continuous neutron sources (reactors) as e.g. at the Hahn-Meitner-Institut.
- If the scattering geometry is left constant, the wavelength of the incoming radiation has to be varied to change the momentum transfer. This technique is frequently used for pulsed neutron sources.

As described in the next section, scattering of neutrons from thin magnetic films allows the investigation of the magnetic structure of single layers and multilayer systems and provides some structural information complementary to other techniques.

The neutron scattering of a film or multilayer can be measured from the total reflection regime up to Q values corresponding to atomic plane periodicities. At the lower values of Q, close to the regime of total reflection, a dynamical theory is required. At higher Q, where the reflectivity is far from unity and extinction of the incident beam is negligible, a simpler kinematical treatment suffices (for a detailed description see e.g. Ref. [Maj91]).

Kinematical Approach

This simple approach basically describes the scattering of waves from a periodic arrangement of scattering centers, such as e.g. atoms or nuclei. The contributions, including amplitudes and phases, of each single scattering center are summed to the final scattering amplitude. Multiple scattering is neglected. This treatment leads to the Bragg equation as a general condition for

diffraction, which states that constructive interference is only observed if the momentum transfer $\vec{Q}$ is equal to a reciprocal lattice vector $\vec{G}$:

$$\vec{Q} = \vec{G} = h\vec{a}_1^* + k\vec{a}_2^* + l\vec{a}_3^*, \tag{5.3}$$

where a_i^* are the reciprocal lattice parameters and $h,\ k,\ l$ are the integer Miller indices.

In the kinematical diffraction limit, the four spin dependent reflectivities $R^{\pm\pm} \propto |F^{\pm\pm}|^2$ and $R^{\pm\mp} \propto |F^{\pm\mp}|^2$, which are proportional to the squares of the corresponding four structure factors F, can in principle be measured. In a particularly useful experimental configuration, which renders the subsequent data analysis more simple, the polarization axis of the neutron spin is directed parallel to the applied field $\vec{H}$ and perpendicular to the vector $\vec{Q}$ of the momentum transfer as shown in Fig. 5.1, where μ_i is the vector of the net magnetization of the ith layer of a multilayer sample at an angle ϕ_i with respect to the applied field $\vec{H}$. If b_i and p_i are the average nuclear and magnetic scattering lengths for the ith atomic plane of an epitaxially grown single crystal superlattice and z_i the position of that plane along the Z-axis (which points in the direction of the momentum transfer $\vec{Q}$), and assuming similar atomic densities for all planes, then the structure factors given above can be described as follows:

$$F^{\pm\pm} = \sum_i (b_i \pm p_i sin\phi_i) e^{iQz_i} \tag{5.4}$$

and

$$F^{\pm\mp} = \sum_i (p_i cos\phi_i) e^{iQz_i}, \tag{5.5}$$

where the superscripts refer to the initial and final neutron spin eigenstates and $\vec{Q}$ is normal to the substrate surface, i.e. parallel to $\vec{z}_i$.

In the reflectometry geometry, the nuclear scattering length b_i and the component of the magnetic scattering length p_i which is parallel to the spin of the incoming neutrons contribute to the non-spin-flip intensity. The spin-flip intensity is of purely magnetic origin. It is caused by interactions between the neutron spin and the perpendicular component of the sample magnetization.

Dynamical Approach

The previously described kinematic theory is not valid for small values of the momentum transfer Q. In this case the continuum approximation of the scattering density holds and extinction is appreciable, i.e. absorption plays an important role and the coherent scattering amplitude then has an appreciable imaginary part. The dynamical method, which is then used to calculate the neutron (and X-ray) reflectivity, is analogous to that used in the solution of thin film optical interference problems. General descriptions of the dynamical theory of neutron reflection in magnetic materials have been given by Mendiratta and Blume [MB76] and Felcher *et al.* [FHC$^+$87] among others. If unpolarized neutrons are used, the dynamical theory leads to the solution of a one-dimensional Schrödinger equation

$$-\frac{\hbar^2}{2m}\frac{d^2}{dz^2}\Psi(z) + V(z)\Psi(z) = E(k_z)\Psi(z) \tag{5.6}$$

(implying the layers to be isotropic within the sample plane and the scattering vector $\vec{Q}$ directed perpendicular to the sample plane) for a neutron plane wave incident on and propagating through a layered continuous medium. $V(z)$ is an effective 'optical' potential, which is a function of the scattering length densities probed by the neutrons at a depth z in a layered medium. The kinetic energy of the neutron is given by

$$E = \frac{\hbar^2 k^2}{2m}, \tag{5.7}$$

where $\vec{k}$ is the neutron wave vector with magnitude $k = \frac{2\pi}{\lambda}$ and m is the neutron mass. Assuming the configuration for specular reflection, the momentum transfer in the z direction can be described by the scattering vector

$$\vec{Q} = \vec{Q}_0 = \vec{k}_f - \vec{k}_i = 2 * k * sin\Theta\ \vec{z} = 2 * k_z\ \vec{z}. \tag{5.8}$$

From Eqs. 5.6 and 5.8, it follows that for neutrons, analogous to light, a refractive index can be defined by

$$n(z) = \frac{k(z)}{k} = \frac{\sqrt{k^2 - \frac{2m}{\hbar^2}V(z)}}{k}, \tag{5.9}$$

where the numerator denotes the perpendicular component of the neutron wave vector as a function of penetration depth into the medium. In Eq. 5.9 the incoming medium was assumed to be vacuum (or air) with $V_{air}(z) = 0$. If the neutron approaches the interface through a bulk medium with $V = V_0$,

$V(z)$ should be replaced by $V(z) - V_0$. A sharp interface between two bulk media with $V_0 < V_1$ acts as a potential barrier for the neutron with a height $\Delta V = V_1 - V_0$. Inside the material with $V = V_1$, the scattering vector is changed according to

$$Q_1^2 = Q_0^2 - Q_C^2, \tag{5.10}$$

where $Q_C = \sqrt{4 * k^2(1 - n^2)}$ is the critical scattering vector. If the neutron kinetic energy $E = \frac{\hbar^2 k_z^2}{2m}$ is less than the potential barrier related to Q_C, total reflection occurs. That is, the reflected intensity $R(k_z) = 1$ for a scattering vector Q_0 smaller than the critical scattering vector Q_C. In that case, Q_1 is imaginary, corresponding to an exponentially damped wave, the evanescent wave. For $Q_0 > Q_c$, the reflectivity for a single surface decays according to the Fresnel law (see thin solid line in Fig. 5.2).

$$R_F(Q_0) = |\frac{Q_0 - Q_1}{Q_0 + Q_1}|^2 = |R_0|^2, \tag{5.11}$$

where R_0 is the Fresnel reflection coefficient for a single surface. Similarly, using the Fresnel transmission coefficient $T_0 = \frac{2Q_0}{Q_0+Q_1}$, the Fresnel transmittivity $T_F = T * T^* \frac{Q_1}{Q_0}$ can be obtained. For $Q_0 \gg Q_c$, the Fresnel reflectivity R_F approaches the asymptotic form

$$R_F(Q_0) \approx (\frac{Q_c}{2Q_0})^4 = \frac{(2m)^2}{(2\hbar Q_0)^4}(\Delta V(z))^2. \tag{5.12}$$

At the interfaces between two media with refractive indices n_0 and n_1, Snell's law holds

$$n_0 * cos\Theta_0 = n_1 * cos\Theta_1. \tag{5.13}$$

This is illustrated for a single surface at the top of the scheme in Fig. 5.1.

As an example, the calculated reflectivity curves for a single SiO_2 substrate surface and for two Ni layers of thicknesses d_m = 2, 20 nm on top of the substrate are compared in Fig. 5.2. The reflectivities are calculated using the program Parratt32 [Bra] based on the Parratt formalism [Par54]. The latter will be briefly outlined in the next paragraph. As expected the reflectivity curve from the single flat substrate surface exhibits a critical scattering vector $Q_C(SiO_2)$. Below Q_C the reflectivity is constant and equal to 1. Above Q_C it drops off approximately as Q^{-4}, as described above. This behavior is usually referred to as Fresnel reflectivity. The reflectivity from a thin layer on top of the substrate is qualitatively different, showing interference fringes above Q_C(Ni), which are due to the interference of waves scattered from the surface and from the interface to the substrate. From the separation of the maxima ΔQ, the film thickness can be estimated as $d_m = \frac{2\pi}{\Delta Q}$. At the reflectivity

maxima, a large fraction of the incoming beam intensity is reflected, while at the minima the waves are trapped within the film boundaries, forming standing waves (constructive and destructive interference).

In the case of thin films and superlattices, scattering from several interfaces has to be considered. For deriving the reflected intensity of a stratified medium, the Parratt formalism uses a recursion method, starting with the lowest layer m, which is infinitely thick, so that the corresponding Fresnel coefficient $R_m = 0$, and then working up to the top surface, where the reflected intensity is $\frac{I_R}{I} = |R_0|^2$. The boundary conditions must be fulfilled at each individual interface and the reflectivities add together to provide the overall reflectivity for a stratified medium.

Defining a phase factor $a_m = e^{iQ_m d_m/2}$ in the middle between two interfaces with Q_m the scattering vector in medium m and d_m the thickness of the mth layer, the equations implied by the boundary conditions can be solved. This leads to the following generalized reflectivities for adjacent interfaces m and $m+1$:

$$R_{m-1} = a_{m-1}^4 \left(\frac{R_{m-1,m} + R_m}{R_{m-1,m} R_m + 1}\right) \tag{5.14}$$

with

$$R_m = a_m^2 \frac{r_m}{t_m}. \tag{5.15}$$

r_m and t_m denote the amplitudes of the reflected and transmitted waves in a medium m. For the interface between the layers m and n the generalized Fresnel coefficient $R_{m-1,m}$ is denoted as follows

$$R_{m-1,m} = \frac{Q_{m-1} - Q_m}{Q_{m-1} + Q_m}. \tag{5.16}$$

Using Eq. 5.14, the Fresnel reflectivity R_F as described above is related to the generalized Fresnel coefficient $R_{0,1}^2$ for a single smooth surface by the following equation:

$$R_F = |R_0|^2 = \left(\frac{r_0}{t_0} a_0^2\right)^2 = \left(a_0^4 R_{0,1}\right)^2 = \left|\frac{Q_0 - Q_1}{Q_0 + Q_1}\right|^2. \tag{5.17}$$

That is, equation 5.11 is obtained again, as should be expected. The reflectivity may be calculated by this recursion scheme developed by Parratt [Par54], which applies no approximation, providing the correct expression for all regions of scattering, and automatically taking absorption into account.

After this general description of the interaction of X-ray and (unpolarized) neutron waves with single films and stratified media, magnetic interactions

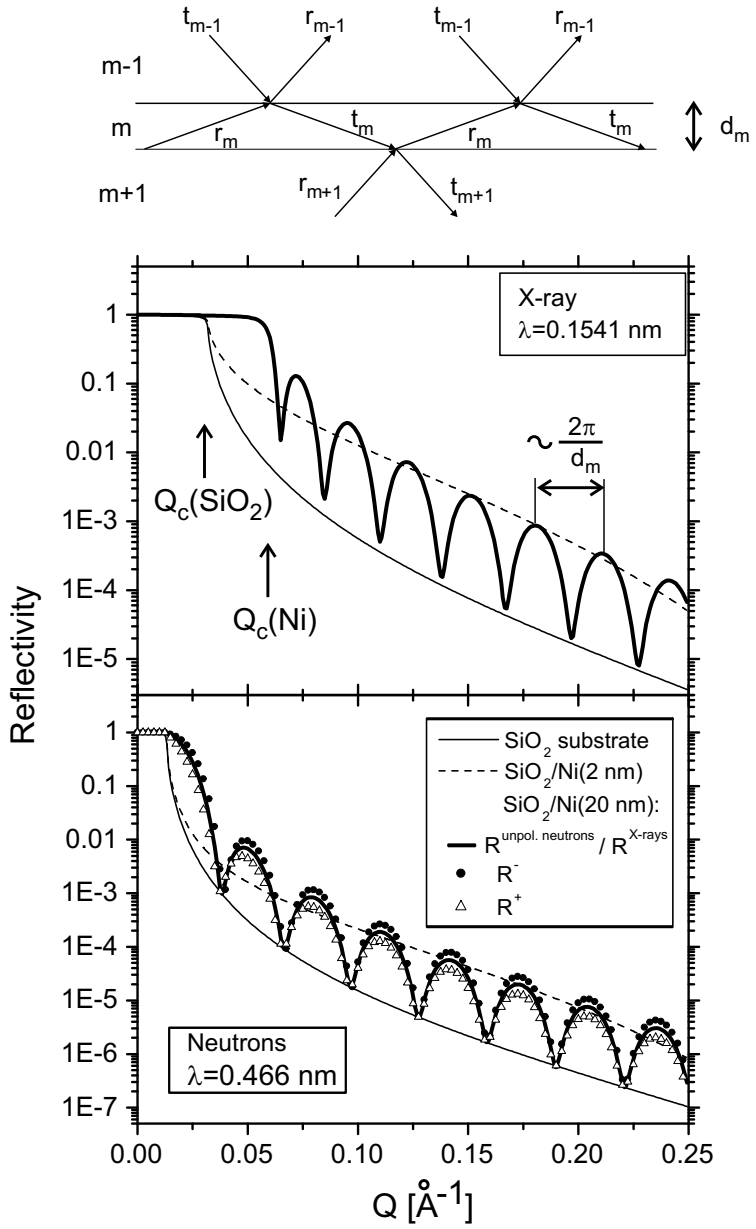

Figure 5.2: Top: Reflection and transmission of waves occurs at all interfaces separating regions of different densities in a layered material; r_m and t_m denote the amplitudes of the reflected and transmitted waves in a medium m. Center and bottom: Calculated X-ray (center) and neutron (bottom) reflectivities from a SiO_2 substrate (thin solid lines) with a Ni layer of thickness d_m; solid lines: $d_m = 2$ nm; dashed lines: $d_m = 20$ nm. The circles and open triangles in the bottom plot represent the reflectivities R^- R^+ calculated for polarized down and up-neutrons for a 20 nm thick magnetically saturated Ni layer on top of a SiO_2 substrate. The spins of the incoming neutrons were assumed to be aligned with the applied field axis.

between polarized neutrons and magnetic (multi-)layers will be treated. Using polarized neutrons, the interaction between the neutrons and matter can be described by an effective potential (V_{eff}) in the Schrödinger equation 5.6 including the nuclear (V_N) and the magnetic interaction (V_M) of the neutrons with the ith layer of a stratified medium:

$$V_{eff}(z) = V_{N,i} + V_{M,i} = V_{N,i} - \vec{\mu}_n \cdot \vec{B}_i(z) = \frac{2\pi\hbar^2}{m}\rho(z) \pm |\vec{\mu}_n \cdot \vec{B}_i(z)|, \quad (5.18)$$

where m is the neutron mass, μ_n the neutron magnetic moment and $\vec{B}$ the magnetic induction. The $\pm$ sign refers to the spin states of the incident neutron. ρ describes the nuclear scattering density given by

$$\rho(z) =< \sum_i N_i b_i >, \quad (5.19)$$

where N_i and b_i are the number density and the coherent scattering length of species i(i.e. the ith layer) and $< ... >$ denotes the average at position z. Neutron absorption is taken into account by the imaginary part of the scattering length $b = b' + ib''$ with $b'' = \frac{k}{4\pi}\sigma_a(k)$, where σ_a represents the absorption cross section. But except for very thick layers and/or strongly absorbing elements, as e.g. Cd and Gd, the absorption can in general be neglected. Corresponding to the nuclear scattering length b_i, a magnetic scattering length p_i can be defined:

$$p_i = \frac{m\mu_n\mu_B\mu_0}{2\pi\hbar^2}|\vec{\mu}_i| = C|\vec{\mu}_i| = \frac{2.695fm}{\mu_B}|\vec{\mu}_i| \quad (5.20)$$

with μ_n the neutron magnetic moment, μ_B the Bohr magneton, μ_0 the magnetic permeability constant and μ_i the magnetic moment of species i in units of μ_B. Assuming in-plane magnetization for a magnetic sample, the magnetization may point in any in-plane direction at an angle ϕ_i with respect to the scattering plane (the applied field is directed perpendicular to the scattering plane, see also Fig. 5.1). The magnetic neutron-sample interaction in the ith layer is described by the magnetic part of the effective potential $V_{M,i}$:

$$V_{M,i} = -\vec{\mu}_n \cdot \vec{B}_i(z) = -4\pi\mu_n\mu_i sin(\phi_i) \quad (5.21)$$

indicating that only the magnetization component, which is parallel to the Y-axis in Fig. 5.1 and to the axis of the incident neutron spin, contributes to the change of the effective potential (Eq. 5.18) that is experienced by the neutron in the sample. The component of the magnetization vector which is aligned in-plane perpendicular to the applied field causes a perturbation of the neutron polarization, which can flip the neutron spin from the (+) to the (−) state or *vice versa*. Therefore the Y-axis, which is parallel to the incident

neutron spins, is called the NSF (non-spin-flip) axis, while the X-axis, which is perpendicular to the incident neutron spins, is called the SF (spin-flip) axis. The spin-flip processes experienced by the neutron while penetrating a magnetic medium have purely magnetic character; they do not occur in coherent nuclear scattering. The neutron plane waves Ψ_+ and Ψ_- for the $(+)$ and $(-)$ states are solutions of the one-dimensional Schrödinger Eq. 5.6. For unpolarized neutrons the magnetic contribution vanishes, because the directional magnetic contributions are averaged. In this case a single one-dimensional Schrödinger Eq. can be solved without the magnetic contribution. In the case of an ideal ferromagnetic thin film with the magnetization vector aligned in-plane and parallel to the incident neutron spins and the applied field, a single one-dimensional equation like Eq. 5.6 has to be solved. If non-collinear magnetic arrangements in a single continuous layer are considered, where spin-flip processes may occur, one has to solve a pair of coupled Schrödinger equations, which may be written as

$$\begin{pmatrix} \frac{d^2}{dz^2} + \alpha_1 & \beta \\ \beta & \frac{d^2}{dz^2} + \alpha_2 \end{pmatrix} \begin{pmatrix} \Psi_+ \\ \Psi_- \end{pmatrix} = \mathbf{0},$$

where

$$\alpha_{1,2} = \frac{1}{4}Q^2 - 4\pi N(b_i \pm p_i sin\phi_i) \tag{5.22}$$

and

$$\beta = 4\pi N p_i cos\phi_i \tag{5.23}$$

with $Q^2 = (\frac{4\pi sin\Theta}{\lambda})^2$ the square of the magnitude of the momentum transfer Q. The diagonal matrix elements describe the NSF scattering, and the off-diagonal elements the SF scattering. In a stratified magnetic multilayer the plane wave functions Ψ_+ and Ψ_- have to fulfill boundary conditions at each interface, when penetrating through the layer structure. This is usually achieved by the transfer matrix method known from optics, which can equally be applied for neutron reflectivity. It allows the determination of the coefficients of the four different cross sections $R^{\pm\pm}$ and $R^{\pm\mp}$, where the last two are usually degenerate. The NSF cross sections can be calculated using the Parratt recursion formalism [Par54], described above. The program Parratt32, developed by C. Braun at the Hahn-Meitner Institut [Bra], based on the Parratt formalism, has been used for the NSF simulations in the present work.

In the bottom plot of Fig. 5.2, simulations of the polarized neutron reflectivities R^- (circles) and R^+ (triangles) which would be obtained from a 20 nm thick magnetically saturated Ni film on top of a SiO_2 substrate are shown as an example. The spins of the incoming neutrons where assumed to

be aligned with the applied field axis. The PNR curves are shifted with respect to the reflectivity obtained for unpolarized neutrons. The intensity contrast between the reflectivities R^- and R^+ is due to the potential difference (see Eq. 5.18) experienced by the up and down-neutrons when interacting with the sample magnetization. This contrast is a direct indicator of the large magnetic polarization along the field axis.

5.2.2 Experimental setup of the V6 reflectometer at the HMI

All PNR experiments in the present work were performed at the V6 reflectometer at the Hahn-Meitner Institut. A scheme of the experimental setup of the reflectometer is given in Fig. 5.3 ([MGKT95]). To analyze the magnetic properties of thin multilayer systems, the reflectivity of polarized neutrons is measured as a function of the momentum transfer $\vec{Q}$. In this work only monochromatic neutrons with $\lambda = 0.466\ nm$ (resolution $\frac{\Delta\lambda}{lambda} = 0.02$) were used and measured by varying the angle Θ_i. The (unpolarized) neutrons with randomly distributed spin orientations, which come from the cold source of the reactor BER II at the Hahn-Meitner Institut, are guided by the neutron guide system to the different experiments. The neutron guides are coated with ^{58}Ni which has a large scattering length providing for a large divergence and thus a high intensity of the neutron beam. The neutrons are monochromatized via Bragg reflection from a graphite crystal in combination with a Be filter. The neutrons with a wavelength $\lambda = 0.466$ nm and its higher orders $\frac{1}{n}$ are reflected from the monochromator. But only the neutrons with $\lambda = 0.466$ nm can pass the Be filter which has a cut-off wavelength of about 0.4 nm. The neutrons are polarized by a FeCo/Si supermirror which reflects the up-neutrons and transmits the down-neutrons. The polarizer at the V6 reflectometer is used in transmission providing down-neutrons. If up-neutrons are needed a spin flipper coil of Mezei-type is used reversing the neutron spins via Larmor precession in a magnetic field. For collimation, the beam passes two sets of computer-controlled cadmium slit systems before it hits the sample at an angle Θ_i. The typical vertical collimation is about 0.01°. The flipper between the two slit systems allows one to invert the polarization of the neutron beam (see also Ref. [MGKT95]). The angle of incidence is usually varied by a precise tilting of the sample surface, potentially with an angular precision of 0.001° relative to the fixed collimated neutron beam. An external field of at least a few gauss has to be applied to the sample in a direction parallel to the quantization axis of the incoming neutrons (requirement for PNR, not required for unpolarized neutrons), or else the neutrons will be depolarized. To maintain the polariza-

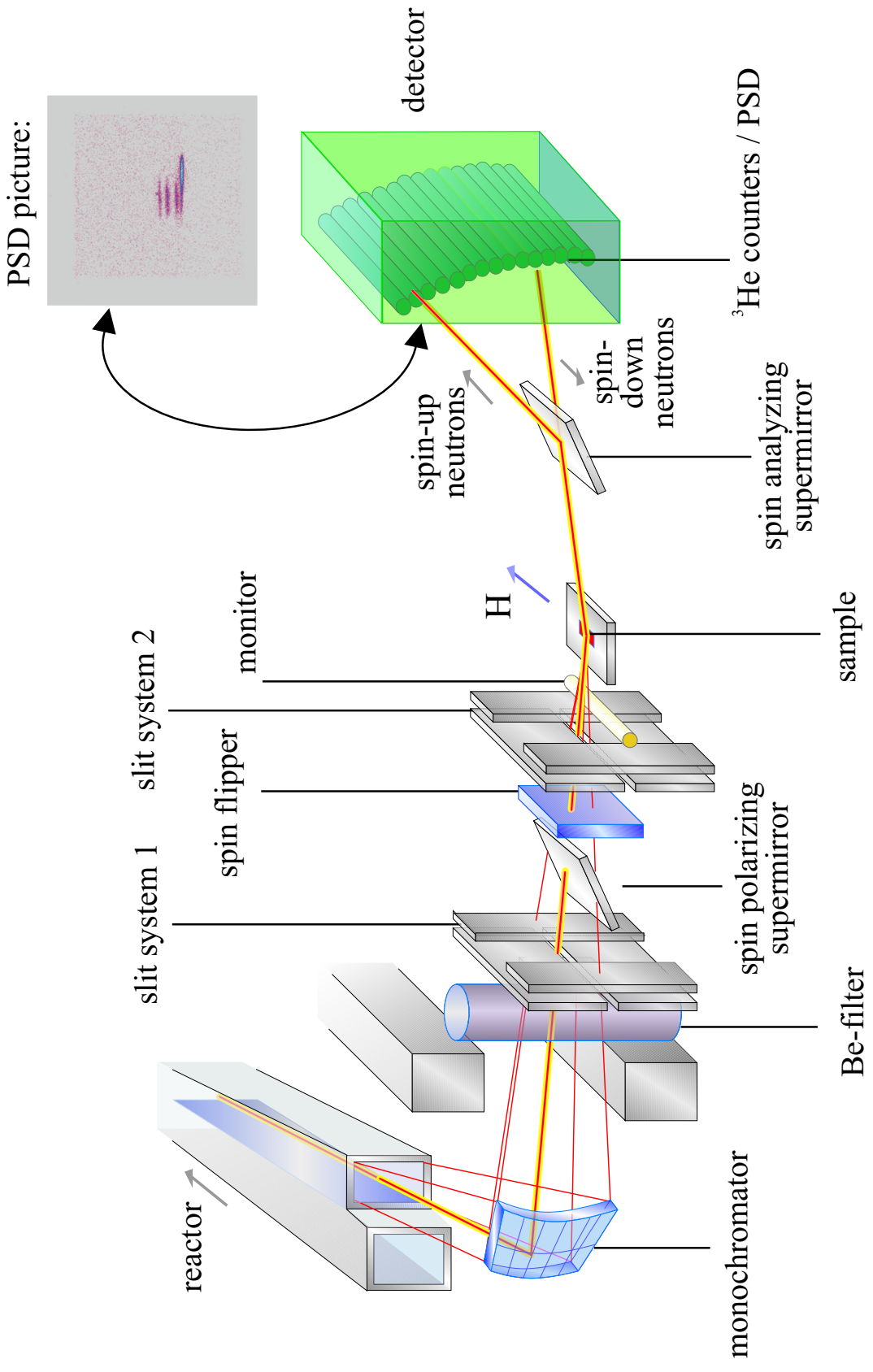

Figure 5.3: Setup of the V6 reflectometer at BER II HMI.

tion throughout the beam path, there are guide fields between polarizer and analyzer, generated by special constructions of permanent magnets supplying a small magnetic field in a particular direction, either parallel or antiparallel to the spin of the incoming neutrons. The neutrons interact with the sample magnetization and the reflected beam at $\Theta_f = \Theta_i = \Theta$ is detected and can be analyzed as a function of the magnetic field, the temperature etc. The detector is an array of 48 ^3He gas detector tubes with an efficiency higher than 90 % for a neutron wavelength of 0.4 nm (detector angular range: 10°). Optionally, a two-dimensional multi-wire position sensitive detector (PSD) (180 mm × 180 mm, resolution 1.5 mm) can be used, which is well suited for the detection of off-specular scattering. The sample–detector distance is variable between 1 m and 3 m. With a spin analyzing supermirror between sample and detector, which reflects only spin-up neutrons, while spin-down neutrons are transmitted, the investigation of magnetic samples with exit beam spin analysis is possible (see Ref. [KPKM95, MGKT95]). When using a polarized incident beam and analyzing the polarization state of the reflected beam, all four spin-dependent reflectivities, non-spin-flip: R^{++}, R^{--} and spin-flip: R^{+-}, R^{+-} can be studied. The typical flux at the sample is $3 \cdot 10^4 \frac{n}{cm^2 s}$ and $1.5 \cdot 10^4 \frac{n}{cm^2 s}$ for polarized neutrons, respectively. The typical accessible reflectivities for samples of a size 10×40 mm^2 is $2 \cdot 10^{-5}$. For measurements at low temperatures the sample is mounted in a closed cycle ^4He cryostat where its temperature can be varied between 10 K and 310 K by a Lakeshore controller.

5.3 Experiments, results and discussion

5.3.1 Motivation

The aim of the present investigations was to study the magnetization reversal processes of a $[Co/CoO/Au]_{20}$ EB multilayer with Polarized Neutron Reflectometry. The investigations were performed at 10 K in the EB state and, for comparison in the unbiased state, at 300 K, i.e. above the Néel temperature (blocking temperature) of CoO. The NSF as well as the SF intensities were measured in order to distinguish between a magnetization rotation and a domain wall movement. Additionally preliminary off-specular PNR measurements will be presented; they can be employed to detect structural and magnetic inhomogeneities (domains) at characteristic magnetic fields.

In context with other experiments performed in this area, the present results further elucidate the character of the magnetization reversal in granular EB systems, which is closely related to the unidirectional nature of the EB effect.

5.3.2 Specular scattering with spin analysis on a $[Co/CoO/Au]_{20}$ EB-multilayer

Θ–2Θ specular reflectivity scans with normal wave vector $|Q|=4\pi \sin\Theta/\lambda$ were recorded for all four cross sections: $R^{+\,+}$, $R^{-\,-}$, $R^{+\,-}$ and $R^{-\,+}$. The two NSF cross sections, (+ +) and (- -), yield information on the nuclear structure and the in-plane magnetization of the sample parallel to the external field axis. For the two SF cross sections, (+ -) and (- +), the neutron polarization is changed due to interaction with the perpendicular magnetization component of the sample. These intensities are exclusively of magnetic origin and correspond to the in-plane magnetization perpendicular to the external field.

In order to explore the reversal processes in the present system, PNR spectra were recorded at different characteristic magnetic fields. Fig. 5.4 shows the measured reflectivity spectra for up- and down-neutrons ($\lambda = 0.466$) over a Q range from 0.01 to 0.13 $Å^{-1}$, when the sample is saturated. The Bragg peaks are narrower for a multilayer than for a comparable bilayer. Therefore the separation of the Bragg peaks for the up- and down-neutrons can be well resolved. The included simulations were performed using the well-known Parratt formalism [Par54, Bra], i) for a magnetically saturated sample where the splitting between the R^{--} and the R^{++} reflectivity is clearly visible (Fig. 5.4 solid lines) and ii) for a non-magnetic sample where $R^{--} = R^{++}$ (Fig. 5.4 thin lines). The reduced intensity at larger Q-values, with respect to the fitted curve, can be attributed to roughness which is not included in the fitting procedure. The difference of the Q-values of the nth and *(n+1)*th order Bragg peaks, ΔQ, is inversely proportional to the thickness of one [Co/CoO/Au] trilayer. Furthermore, it should be noted that for the NSF reflectivities the peak position described in case ii) is identical to that of a magnetic sample with a magnetization rotated coherently by 90 degrees with respect to the external magnetic field. In the ideal case of a coherent magnetization rotation, the Bragg diffraction peaks in the NSF spectra would shift from one saturation state (R^{--}) to the other (R^{++}), passing through the non-magnetic Bragg peak position during the reversal process.

Neutron reflectivity profiles corresponding to three characteristic fields in the 1st cycle of the magnetization curve of the biased state (at 10 K) are shown in Fig. 5.5: in magnetic saturation (A) and close to the coercive fields $H_{CA} \sim -883$ Oe (B) and $H_{CP} \sim 110$ Oe (D). The 4th profile shown in the bottom plot was monitored close to the reduced coercive field $H_{CA} \sim -599$ Oe (G) of the 2nd cycle (training cycle) (see also Ref. [tVBF$^+$00]). The field values corresponding to the 1st cycle of the magnetization curve have also been marked by circles in Fig. 4.6 in chapter 4, where the characteristic EB properties of the present multilayer were treated. For clarity the magnetic

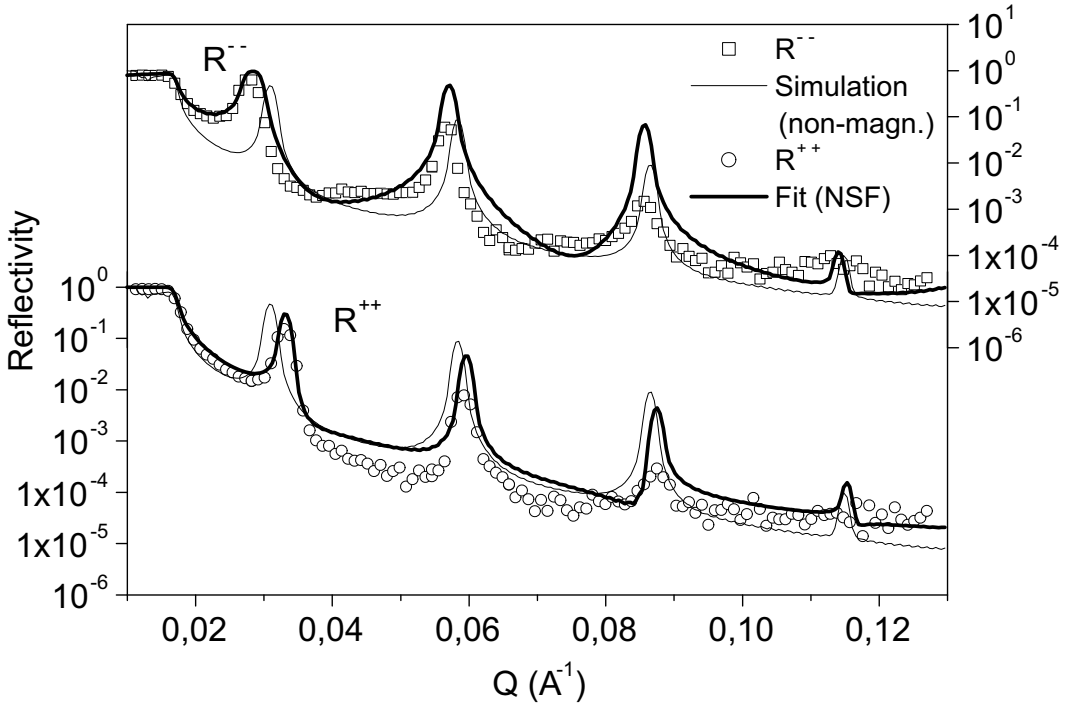

Figure 5.4: Reflectivity spectra for up-neutrons (open circles) and down-neutrons (open squares) obtained from a $[Co/CoO/Au]_{20}$ multilayer and the corresponding fits for the sample's saturated state, measured at 2973 Oe. The solid lines are fits to the reflectivities R^{++} and R^{--} for the case of saturation, and the fine line simulates the case of a non-magnetic sample or a sample with its magnetization perpendicular to the external field, respectively.

hysteresis loop as measured by SQUID is plotted beside each PNR plot. The corresponding magnetic field is marked by a boldface circle. Solid lines are fits to the NSF reflectivity.

The present PNR profiles are focused on a small range of wave vector values $\vec{Q}$ featuring only one characteristic peak. For magnetic saturation (Fig. 5.5A), each of the two NSF reflectivity profiles is characterized in the Q range considered by one dominant peak. Depending on the different sign of the magnetic contribution to the neutron scattering potential, the peak positions in the (++) and the (- -) reflection profiles are clearly separated from each other. Apart from a background of less than 10^{-3}, there is no significant contribution in the SF profiles, which is expected for the sample magnetization aligned along the external field. For $H \approx H_{CA}$ (Fig. 5.5B), both NSF profiles now clearly exhibit two peaks at the same positions as observed in Fig. 5.5A. Obviously, the sample magnetization now consists mainly of domains pointing either par-

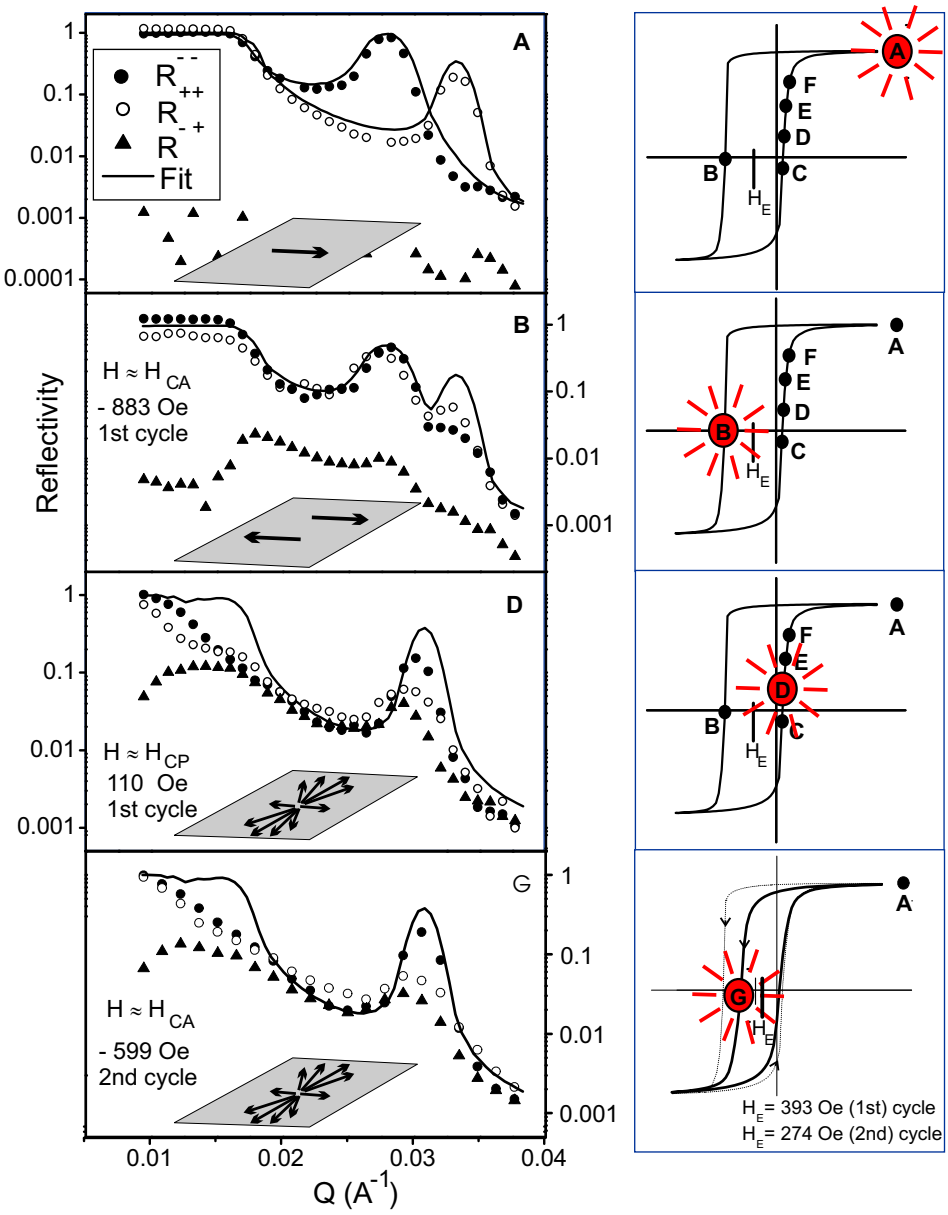

Figure 5.5: Left: Non-spin-flip (open and closed circles) and spin-flip (triangles) PNR profiles obtained from the $[Co/CoO/Au]_{20}$ multilayer in the biased state at 10 K. The PNR profiles show $\Theta - 2\Theta$ scans recorded at different characteristic magnetic fields: (A) in magnetic saturation, (B) at the field close to coercive field $H_{CA} \approx -883\ Oe$ the magnetization reversal is dominated by domain wall movement, (C) at the field close to coercive field $H_{CP} \approx 110\ Oe$ the magnetization reversal is dominated by rotation processes, (D) during the second (training) cycle, at the field close to coercive field $H_{CA} \approx -599\ Oe$ the magnetization reversal is again dominated by rotation processes (see text). Right: Magnetic hysteresis loop measured by SQUID at 10 K in the EB state of the multilayer. The dots on the SQUID curves mark the characteristic fields where PNR spectra were taken.

allel or antiparallel to the applied field. That is, almost identical cross sections for (++) and (- -) neutrons correspond to an almost equal distribution of domains with parallel or antiparallel magnetization. This behavior is further illustrated by the curve fit which represents an intuitive model, simply adding half of the calculated intensity of the (++) and (- -) profiles of the saturated state (Fig. 5.5A). The model does not account for SF processes and diffuse scattering from domains. The resulting net magnetization of the observed domain configuration is zero. The corresponding SF profile in Fig. 5.5B indicates a small amount of magnetization perpendicular to the applied field. But a reflectivity of only 10^{-2} implies that either the degree of rotation is minimal or only a small part of the total multilayer magnetization has been rotated. It can therefore be concluded that the observed configuration with magnetization pointing either parallel or antiparallel to the applied field originates from a reversal which is mainly due to domain wall motion. This is further supported by additional reflectivity profiles on the decreasing field branch with external fields slightly higher or lower than $H = -883$ Oe $\approx H_{CA}$ of Fig. 5.5B, as illustrated for $R^{-\ -}$ in Fig. 5.6. The reflectivity profiles in Fig. 5.6 reveal two peaks at fixed positions but with varying intensities corresponding to an increasing or decreasing number of domains with either parallel or antiparallel magnetization.

Close to the opposite coercivity H_{CP} (Fig. 5.5D), both NSF profiles clearly show only one dominant peak at a changed position (which is between the peak positions in Fig. 5.5A and Fig. 5.5B). This position is very close to the peak found by the simulation when only the nuclear contributions to the neutron potential are included (solid line in Fig. 5.5D). Additionally, the reflectivity in the SF profile is of the same magnitude as in the NSF profiles. This unambiguously proves that the main part of the magnetization has been rotated in the plane of the sample towards the direction perpendicular to the external field. In contrast to the behavior found for $H \approx H_{CA}$, the reversal mechanism in the increasing field branch ($H \approx H_{CP}$) is obviously due to rotation, while a certain amount of off-specular reflection was also recorded by a position-sensitive detector (see also next section). Spin-dependent diffuse scattering can be considerable in EB systems [tVBF$^+$00]. Furthermore, a closer inspection of the reflectivity spectrum reveals significant intensity losses at Q values close to the total reflection edge, as well as a broadening of the Bragg peak. Together with the observation of off-specular scattering, this observation suggests that the magnetization at H_{CP} is not coherently rotated, but rather breaks into domains with a dispersion of magnetic orientations (as schematically illustrated in the bottom part of each plot). A ferromagnetic domain distribution during the magnetization reversal in a thin Co/CoO bilayer was recently reported by Lee *et al.* [LtVF$^+$02].

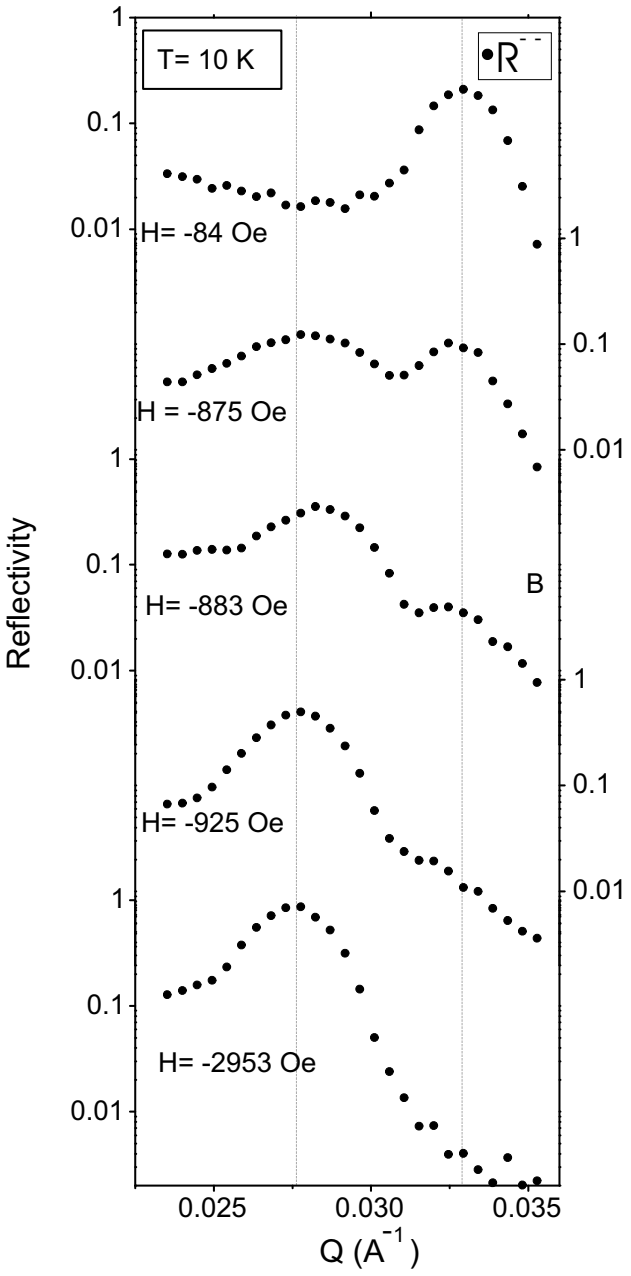

Figure 5.6: Non spin flip PNR profiles (down-neutrons) obtained from the $[Co/CoO/Au]_{20}$ multilayer at 10 K: $\Theta - 2\Theta$ scans at different magnetic fields in the vicinity of the coercive field H_{CA} indicating growth of domains with magnetization either parallel or antiparallel to the applied field (see text).

For comparison to the results obtained at the coercive fields during the 1st cycle, Fig. 5.5G shows the reflectivity at the coercive field H_{CA} of the 2nd cycle. The corresponding SQUID curve on the right side of the plot reveals strong effects of training with cycling of the magnetic field. The EB shift and the coercivities are reduced and no sudden reversal at H_{CA} is observed anymore. The PNR spectrum of this state shows similar features as for the magnetization reversal at the coercive field H_{CP} of the 1st cycle, i.e. the magnetization reversal of the trained sample is dominated mainly by magnetization rotation. This result confirms the result obtained by Velthuis *et al.* [tVBF$^+$00].

In order to compare the reversal processes present in the biased state at 10 K and in the unbiased state at 300 K, two sets of PNR reflectivity curves (non-spin-flip) around the first-order Bragg peak are shown in Fig. 5.7. The figure shows PNR curves for five different applied fields on the increasing branch of the magnetization curve, corresponding to five different magnetization states. The left-hand side of this figure shows measurements at 10 K for the biased state, while the right-hand reflectivities were recorded at 300 K for the sample's unbiased state.

Before the magnetic field was increased in small steps, the sample was saturated at negative fields. A magnetization reversal, which is characterized by domain rotation, can be observed for applied fields close to the coercive fields ($H_{CP} = +110$ Oe at $T = 10$ K and $H_{CP} = +6.5$ Oe at $T = 300$ K). In-plane rotations of the magnetization are detected not only by an increased intensity in the SF channels, but also in the NSF spectra. As opposed to the situation at the decreasing field branch close to H_{CA}, the NSF profiles reveal one dominant peak at a position close to the simulated peak position for the non-magnetic case corresponding to only the nuclear contributions of the neutron potential. With increasing fields this peak shifts towards a smaller (for R^{--}) Q value, reaching its saturation value for the case of magnetic saturation (shown in Fig. 5.7a for an external field of 2973 Oe). The magnetic contribution of the NSF reflectivity profiles to the neutron potential reaches its maximum value at magnetic saturation.

The rotation process can virtually be followed as a function of the external field by the gradual peak shift towards the saturation position (Fig. 5.7A and a) because NSF cross sections are sensitive only to the projection of the magnetization parallel to the field direction. The behavior is almost identical in both cases, i.e. for H_{CP} and for the reversal processes at 300 K in the unbiased state.

At 6.5 Oe (Fig. 5.7b, 300 K) and 109.7 Oe (Fig. 5.7C, 10 K), a high SF signal can be observed together with a Bragg peak position for the down-neutrons which is close to the simulated peak position for the non-magnetic case. At 10, 12.5 and 14.7 Oe (300 K) and at 135.3, 159 and 234 Oe (10 K)

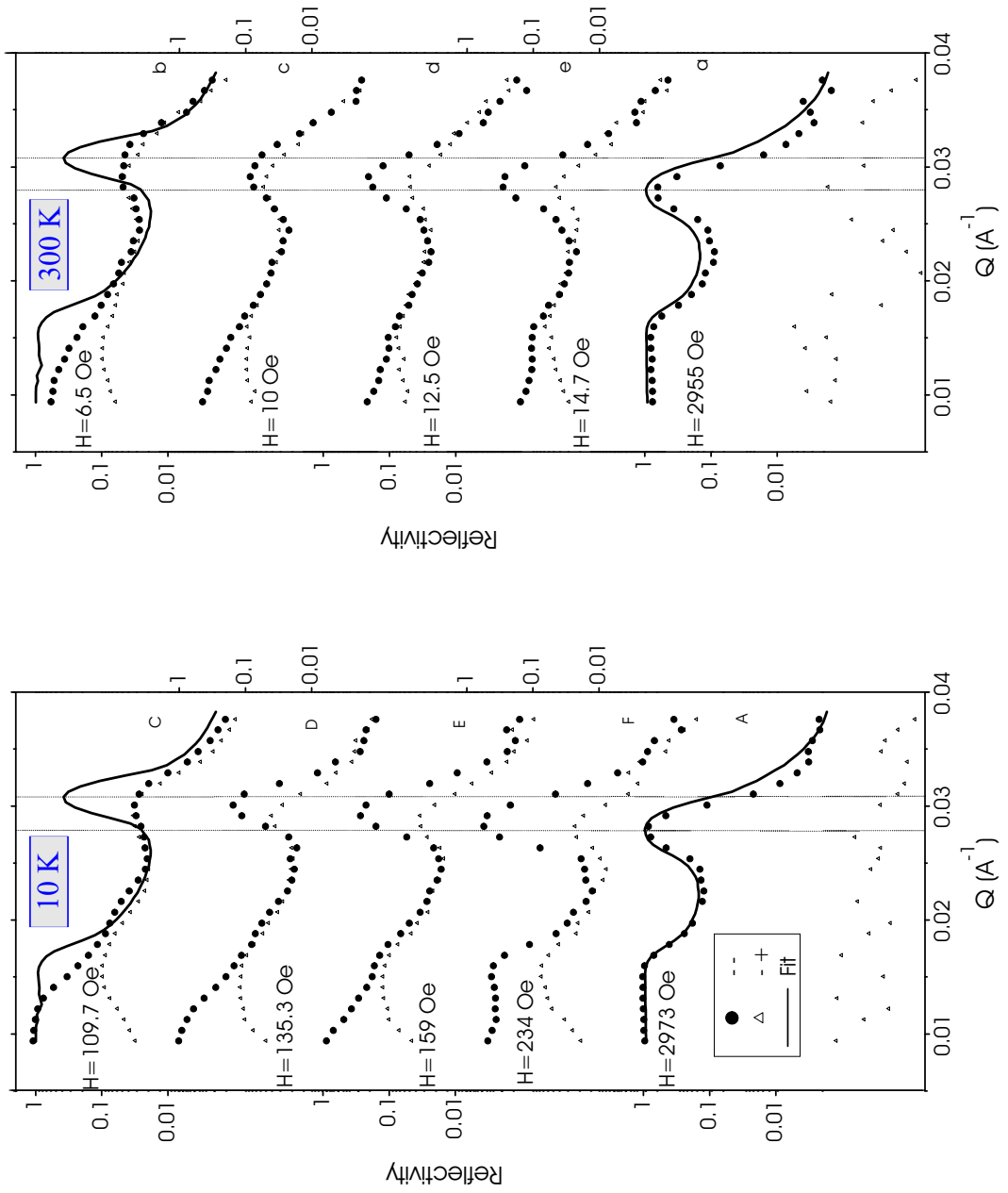

Figure 5.7: PNR (NSF=circles; SF=triangles) profiles for the $[Co/CoO/Au]_{20}$ multilayer: $\Theta - 2\Theta$ scans at different magnetic fields close to the coercive field H_{CP} at room temperature (right) and at 10 K (left), where magnetization rotation was observed. The solid lines are fits to the data for the case of magnetic saturation (bottom fit) and for the case of either a non-magnetic sample or a sample with its magnetization perpendicular to the neutron spin axis and to the applied field (close to coercive field) (top fit).

(Fig. 5.7c, d and e), the R^{--} Bragg peak shifts towards smaller Q values, reaching its saturation value for the case of magnetic saturation (in Fig. 5.7a shown for external fields of 2973 Oe and 2955 Oe respectively). The simulated reflectivity curves are in good agreement for saturation, where no spin-flip signal occurs. For large SF signals (as observable in Fig. 5.7b-e and C-F), the simulated curve is no longer valid because the Parratt formalism does not take into account SF contributions and off-specular scattering. Please note that no occurrence of an additional peak can be observed, which would indicate domain wall movements as described above.

The experimental findings are compared to the results obtained by SQUID magnetometry on the same multilayer (using a small sized sample which was prepared together with the large "PNR"sample).

A magnetic hysteresis loop measurement (SQUID) of the multilayer, performed at 300 K, shows no shift and has small coercivities H_C of less than 20 Oe, which is typical for thin films with soft magnetic properties [GR00b, GR00a]. At T=300 K, which is sufficiently above the blocking temperature for EB in this particular type of Co/CoO system ($\sim$ 200 K), there is virtually no magnetic coupling between Co and CoO (unbiased state) [GR00b]. In addition, PNR measurments performed at T = 300 K (in the unbiased state) reveal that the magnetization reversal is mainly due to rotation on both sides of the hysteresis loop.

In contrast, the low temperature SQUID measurement reveals the strong exchange anisotropy (EB field: $H_E = -393$ Oe at 10 K, see Fig. 4.6 in chapter 4) of the sample as well as an asymmetric shape of the hysteresis loop. The latter indicates that the magnetization reversal processes on opposite sides of the hysteresis loop are different. The shape of the hysteresis curve provides the first information on the underlying reversal mechanisms: For decreasing fields, magnetization remains in saturation up to a high coercive field $H_{CA} = -895$ Oe (antiparallel H_{COOL}) before a sudden reversal takes place. On the opposite side, at $H_{CP} = +110$ Oe (parallel H_{COOL}), the return to saturation for increasing fields is characterized by a rounded edge of the hysteresis loop.

PNR measurments performed in the biased state give more concrete information about the underlying reversal mechanisms, being sensitive to the in-plane direction(s) of the magnetization vector(s) in the sample.

In summary, a drastic change in the magnetization reversal processes in a $[Co/CoO/Au]_{20}$ multilayer has been observed. For the unbiased state (T= 300 K), reversal is due to rotation on both sides of the hysteresis loop. For the biased state (T=10 K), rotation is the main mechanism only for increasing fields. On the decreasing field branch, which is the direction opposite to the bias (cooling field), the mechanism changes to domain wall motion. That is,

for the EB state the AFM affects the reversal of the FM only in the direction opposite to the bias whereas for the transition back into the bias direction, the AFM appears not to have any significant effect. Therefore a drastic change of magnetic behavior, observed exclusively opposite to the pinning direction, can be expected for a system with strong unidirectional anisotropy, which is characterized by only one prominent direction being the cooling field direction.

5.3.3 Off-specular (diffuse) scattering from structural and magnetic inhomogeneities

From the results obtained from specular PNR experiments on a $[Co/CoO/Au]_{20}$ EB-multilayer, significant intensity losses in the specular reflection profiles have been observed at characteristic magnetic fields during the magnetization reversal processes. The missing intensity was presumed to be re-distributed in the off-specular scattering region due to scattering from magnetic domains. In order to detect the off-specular scattering, preliminary PNR experiments were carried out using a two-dimensional Position Sensitive Detector (PSD).

In the following paragraph the scattering mechanisms leading to off-specular scattering are outlined qualitatively. Subsequently the scattering geometry and the creation of a two-dimensional intensity map representing a certain region of reciprocal space are briefly described. Finally the off-specular PNR results obtained for the present $[Co/CoO/Au]_{20}$ EB-multilayer will be presented and qualitatively interpreted.

Some general remarks about off-specular scattering

Ideal (magnetic) multilayers composing of layers with a perfectly homogeneous in-plane structure would cause only specular neutron reflections (in magnetic saturation) in the low scattering-vector region near multilayer Bragg peaks.

By using specular PNR, magnetic and structural information about the one dimensional scattering length density profile perpendicular to the surface is obtained, which is directly related to the chemical profile.

However, in many multilayer structures interdiffusion or a reasonable amount of roughness exists, caused by in-plane inhomogeneities. The specular PNR reflectivity of a layer system with a rough surface or rough interfaces is somewhat reduced in comparison to a perfectly smooth layer system with ideally sharp interfaces. From the specular reflection profiles, a rough interface with sharp local chemical gradients cannot be distinguished from an overall smooth interface with interdiffusion, since the reflectivities are averaged over large lateral areas of the sample. In the case of a rough interface the lost intensity is re-distributed into the off-specular diffuse region of scattering, while a homogeneous interface with interdiffusion does not give rise to diffuse scattering of the neutrons. The distribution of irregularities in rough interfaces may be arbitrary or there might exist some vertical correlations between inhomogeneities of adjacent layers. The latter is called correlated or conformal roughness. That is, the irregularities are replicated to some extent from one interface to the next, i.e. they exhibit the same vertical periodicity as the multilayer.

Conformal roughness can be detected by using a PSD detector, which

records specular ($\Theta_i = \Theta_f$) and off specular ($\Theta_i \neq \Theta_f$) scattering at the same time. A (Θ_i, Θ_f) intensity map can be created in which the intensity is plotted as a function of Θ_i and Θ_f. In a (Θ_i, Θ_f) intensity map usually the intensity is projected onto the (Θ_i, Θ_f) plane using different colors or grey tones for the intensity contrast.

If conformal roughness is present, the multilayer Bragg peaks are replicated in the off-specular region leading to off-specular streaks perpendicular to the specular ridge of a (Θ_i, Θ_f) intensity map. These streaks, caused by vertically correlated inhomogeneities, exhibit the same periodicity as the multilayer Bragg peaks, as shown schematically in the top left sketch of Fig. 5.8 [Zab94b, Kor91]. As illustrated in the top right sketch of Fig. 5.8 for the case of a sinusoidal waviness passing vertically through the multilayer, the conformal roughness can be characterized by a lateral coherence length ξ. ξ is inversely proportional to the frequency of the interfacial irregularities and is assumed to be smaller than the coherence length of the neutron radiation projected into the surface ($\approx 10 - 300$ μm, depending on the incident angle of the neutron beam), so that interference is possible. Perfectly periodic lateral inhomogeneities of the interface would appear as discrete peaks extending at periodic distances perpendicular to the specular ridge of a (Θ_i, Θ_f) intensity map (e.g. see [TBF01]). But usually the interfacial roughness has to be described by a distribution of different lengths deviating from the coherence length ξ, which leads to the streaks extending perpendicular to the specular ridge of a (Θ_i, Θ_f) intensity map.

In contrast to conformal roughness, non-conformal roughness would manifest itself in a uniformly distributed intensity. The sketches of two schematic intensity maps in Fig. 5.8 illustrate the difference between conformal (top) and non-conformal (bottom) roughness.

Furthermore, additional diffuse streaks might appear when $\Theta_i = \Theta_C$, $\Theta_i = \Theta_1$ or $\Theta_f = \Theta_C$, where Θ_C is the critical angle of total reflection and Θ_1 is the angle of the first-order Bragg Peak. The diagonal solid lines in Fig. 5.8 indicate Θ_i=Θ_C and Θ_f=Θ_C, where the diffuse scattering is amplified by the transmittivity function appearing as peaks in rocking scans, which are referred to as Yoneda peaks or angels' wings [Yon63, Zab94b]. The regions of reciprocal space corresponding to angles Θ_i, Θ_f smaller than the critical angle of total reflection Θ_C are largely inaccessible to reflectivity measurements because they are either shadowed or the scattering vector becomes imaginary. The dashed lines in the top intensity distribution for correlated interfaces in Fig. 5.8 at Θ_i=Θ_C and Θ_i=Θ_1, indicate where further ridges might occur, which are also observable as peaks in rocking scans. They are attributed to several dynamical scattering effects. Multiple scattering possibly accounts for peaks causing diagonal ridges in (Θ_i, Θ_f) maps at $\Theta_i = \Theta_1$ and Θ_2 by a mechanism in which

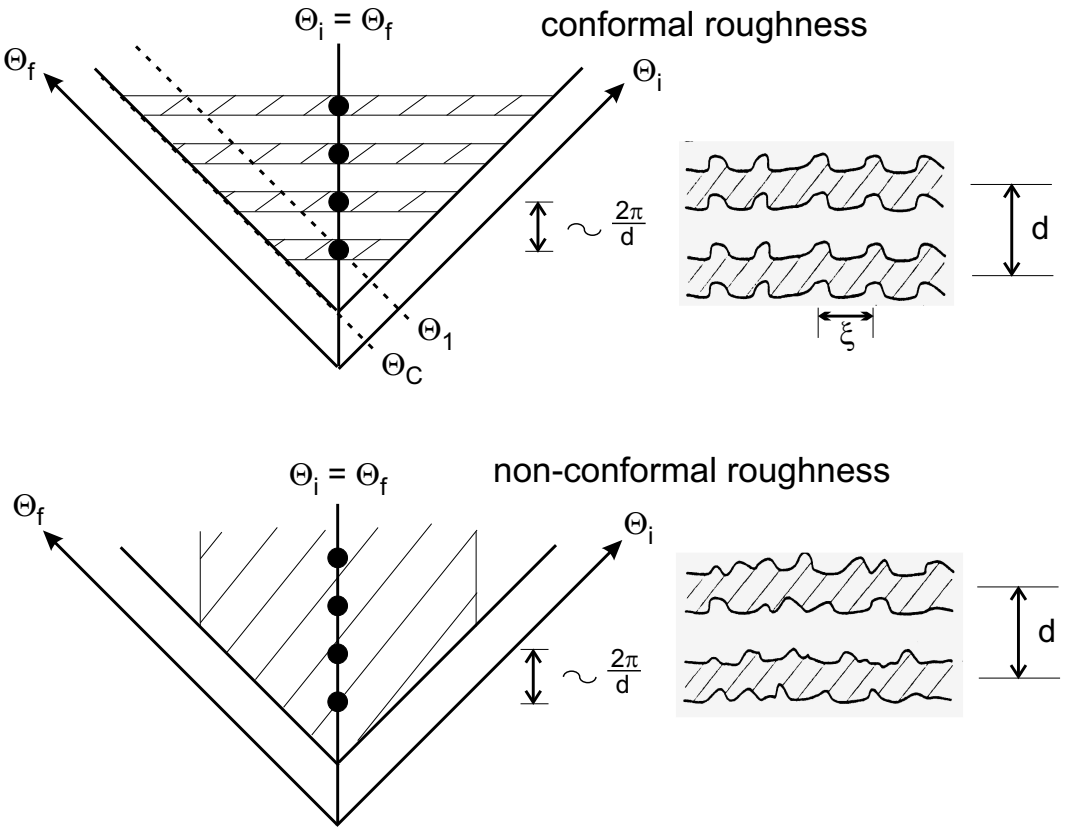

Figure 5.8: Sketch of interfaces in a multilayer showing conformal roughness (top, right) caused by irregularities which are replicated to some extent from one interface to the next. On the left-hand side of the sketch the expected intensity distribution is illustrated. The diffuse intensity exhibits maxima at the satellite peak positions (solid dots) and streaks out in the direction perpendicular to the specular ridge. In the bottom sketch (right), uncorrelated rough interfaces are illustrated. The expected intensity distribution of the corresponding diffuse scattering is shown on the left-hand side. The incoherent superposition of the scattering from each interface does not cause any structure parallel to the specular ridge. The diagonal solid lines indicate Θ_i=Θ_C and Θ_f=Θ_C, while the dashed lines in the upper intensity distribution for correlated interfaces show Θ_i=Θ_C and Θ_i=Θ_1. At these angles the diffuse scattering is amplified, which can also be observed from additional peaks in rocking scans (see also Ref. [Zab94b, Kor91]).

non-specular $q_x = \frac{2\pi}{\lambda}(cos\Theta_f - cos\Theta_i)$ components couple the first and second order Bragg conditions. For further details see Ref. [Zab94b, Kor91] and references therein.

While the theory for conformal roughness is presently still under development, this type of roughness can be experimentally recognized in scans parallel to the specular ridge. If the off-specular scattering follows the shape of the specular scattering, the pattern of any irregularities is replicated from interface to interface. The diffuse 'Bragg' sheets extending perpendicular to the specular ridge show the same periodicity as the multilayer Bragg peaks.

In magnetic multilayers, in addition to the chemical roughness (e.g. a lateral waviness), off-specular or diffuse scattering can be caused by magnetic roughness (e.g. domains, domain distributions or magnetic dots [TBF01]). The magnetic roughness changes with the applied field and it is therefore distinguishable from chemical roughness.

Thus performing off-specular scattering experiments with polarized neutrons provides useful information about magnetic domain formation during magnetization reversal processes.

Off-specular scattering geometry and (Θ_i, Θ_f) intensity maps

As schematically illustrated in Fig. 5.9, the off-specular scattering caused by inhomogeneities of rough interfaces can be detected at a scattering angle Θ_f with respect to the sample surface. Θ_i is the angle between the incoming neutron beam and the sample surface.

The scattering geometry for off-specular scattering with a PSD detector is illustrated in Fig. 5.9. On the right-hand side of this figure a PSD image is plotted which was detected for a particular angle Θ_i of the incident beam. On the left of the PSD image the intensity of that image is projected into the X direction, i.e. the intensity is plotted as a function of the channel numbers in X direction, which are directly related to the scattering angles Θ_f. The X axis can be rescaled by setting the channel number, which corresponds to the specular reflected beam, to $\Theta_f = 0$. Joining the intensity plots for successive Θ_i into a three-dimensional matrix, where the elements are the measured intensity values, allows imaging of the scattered intensities as a function of the incidence angle Θ_i and the scattering angle Θ_f. Usually the intensity (the "3rd dimension"in the matrix) is projected into the (Θ_i, Θ_f) plane. A (Θ_i, Θ_f) intensity map represents a region of reciprocal space, providing the possibility of visualizing the specular and off-specular scattering from vertical and lateral, chemical and magnetic structures of a multilayer system at the same time. The angles Θ_i and Θ_f can easily be converted into the reciprocal space coordinates $q_x = \frac{2\pi}{\lambda}(sin(\Theta_f) + sin(\Theta_i))$ and $q_z = \frac{2\pi}{\lambda}(cos(\Theta_f) - cos(\Theta_i))$. Similar to a

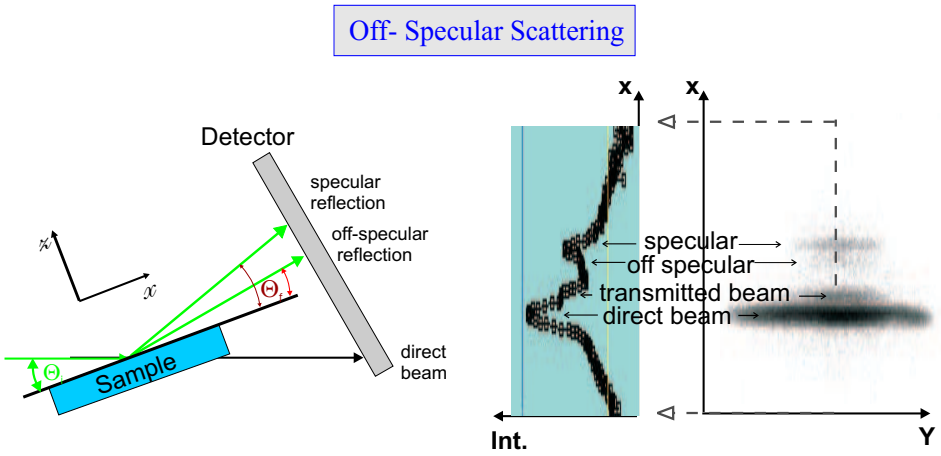

Figure 5.9: left: Schematic outline of the scattering geometry for polarized neutrons illustrating the mechanism for off-specular scattering. Right: detection of off-specular scattering with a Position Sensitive Detector (PSD)

(Θ_i, Θ_f) intensity map, it is possible to create a (q_x, q_z) intensity map, where the intensity is plotted as a function of q_x and q_z. Both kinds of intensity maps can be found in the literature.

It has to be noted, that the experiments presented in this work were not sensitive to in-plane structures along the Y-direction. In order to provide enough signal to noise the whole sample had to be illuminated, which results in a very poor collimation in the Y-direction.

All (Θ_i, Θ_f) intensity maps included in this work were generated as described above using a color scheme from dark blue for the background noise, through light blue, through orange to red for the maximum intensity of total reflection.

Off specular scattering results on a [Co/CoO/Au] EB-multilayer

In addition to the specular PNR measurements, a series of off-specular experiments on the [Co/CoO/Au] multilayer is presented. The experiments were carried out at 10 K with the sample in the biased state. The off-specular scattering was monitored at different characteristic magnetic fields: in magnetic saturation and close to the coercive fields, where the magnetization reversal takes place. As already described in the previous section, a reasonable loss of intensity (with respect to magnetic saturation) for the specularly reflected neutrons was observed at applied fields close to the coercive field on the increasing field branch of the magnetic hysteresis (close to H_{CP}). The lost intensity cannot be attributed only to the highly increased spin-flip contributions at this

field. The missing intensity is presumed to be off-specularly scattered from magnetic domains.

The intensity maps in figure 5.10 represent the polarized intensity for antiparallel (-, top) and parallel (+, bottom) incident neutron spins. The angle of the incoming neutron beam Θ_i was increased from 0.2° to 2.6° and the [Co/CoO/Au] multilayer was magnetically saturated. The (-)/(+) intensity profiles of the specularly reflected neutrons, as measured by the preceding specular PNR experiments, are located at the center of the page between the intensity maps. The specularly reflected intensity profiles (specular ridge, $\Theta_i = \Theta_f$) are indicated as dashed lines located within a transparent rectangle. The increased intensity of the multilayer Bragg peaks can be recognized from the color contrast in the map. Comparing the (Θ_i, Θ_f) maps for (-) and (+) incident neutron spins, the difference of the multilayer Bragg peak positions is clearly distinguishable. It should be noted that no spin analysis was performed, i.e. $R^- = R^{--} + R^{-+}$ and $R^+ = R^{++} + R^{+-}$ are measured. Obviously the present off-specular intensity maps do not reveal in-plane rotations of the magnetization. Apart from the ridge at $\Theta_i = \Theta_f$, the most prominent non-specular features are diffuse streaks extending perpendicular to the specular ridge and crossing the latter at the Bragg peak positions. The existence of the streaks implies a coherent interference of the scattered neutrons and can be attributed to conformal roughness (see also [Zab94b, Kor91]).

This experimental finding is consistent with TEM images of the same multilayer, as presented in chapter 3, revealing a waviness of the trilayers which is transmitted from the bottom to the top of the multilayer.

Furthermore, additional diffuse streaks appear at $\Theta_i = \Theta_1$ and $\Theta_i = \Theta_2$, where Θ_1, Θ_2 are the angles of the first- and second-order Bragg peaks. The ridges of diffuse intensity observed under this condition are attributed to several dynamical effects. Multiple scattering possibly accounts for these intensity peaks appearing as diagonal ridges in the (Θ_i, Θ_f) intensity map along the directions defined by $\Theta_i = \Theta_1$ and $\Theta_i = \Theta_2$. They might be caused by a mechanism in which non-specular $q_x = \frac{2\pi}{\lambda}(cos\Theta_f - cos\Theta_i)$ components couple the first- and second-order Bragg conditions. In X-ray scattering experiments on a W/C multilayer, a similar ridge of diffuse intensity has been observed for Θ_i equals Θ_1 [Kor91].

None of these features would be observed for a multilayer structure with perfectly homogeneous layer planes.

At $\Theta_i = \Theta_C$, i.e. the incident angle equals the critical angle Θ_C of total reflection, a ridge of weakly increased intensity can be observed, which is due to Yoneda scattering, as described in the first paragraph of this section [Yon63, Zab94b].

In figures 5.11 and 5.12, four (Θ_i, Θ_f) intensity maps are shown for the

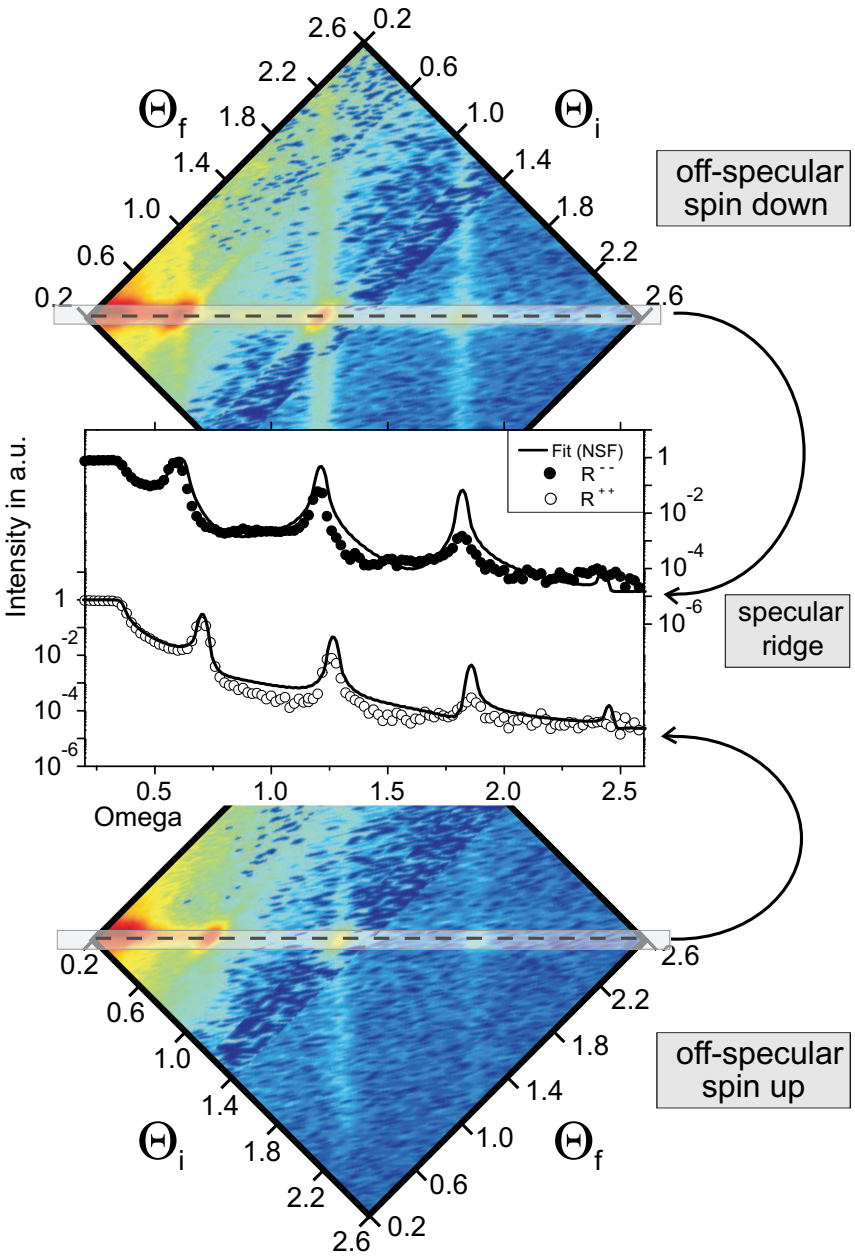

Figure 5.10: (Θ_i, Θ_f) intensity maps for down (top) and up (bottom) neutrons scattered from a [Co/CoO/Au] multilayer in magnetic saturation. The spins of the incident neutrons are aligned along the applied field axis. Dashed lines indicate the specular ridge. Centered between the two intensity maps the specular reflectivities ($\Theta - 2\Theta$ scans) for up (open circles) and down (closed circles) neutrons are plotted together with the corresponding fit curves (solid lines). The edges extending parallel to the Θ_f axis at $\Theta_i = 0.6, 1.2, 1.4$ have an experimental origin: at these angles the counting time was changed in order to optimize the signal-to-noise ratio. At $\Theta_i = 1, 4$ additionally the opening of the slits had to be increased. For these reasons the statistical error from the data is changed, resulting in the observed edges, in spite of data normalization.

case of polarized incoming (-) neutrons. They were recorded at four different characteristic magnetic fields. The intensity maps in the selected Θ range feature the 1st and 2nd order Bragg peak. Below each polarized intensity map the line scans of the specularly reflected intensity are plotted for incoming (-) and (+) neutrons. Below the specular reflectivity plots the magnetization curve of the multilayer in the biased state, as measured by SQUID, is given. For clarity the position in the hysteresis where the neutron data was recorded is marked by a boldface circle.

Fig. 5.11 represents the intensity distribution for the case of magnetic saturation (left) and close to the coercive field H_{CA} at -883 Oe (right). As measured by specular PNR with spin analysis, the magnetization reversal at this coercive field was found to be dominated by the growth of domains with magnetization either parallel or antiparallel to the applied field. In comparison with the case of magnetic saturation, the off-specular scattered intensity at H_{CA} is increased in particular in the small angle region; that is the region of total reflection up to the 1st order multilayer Bragg peak. The intensity around the specular rod is altogether increased in this region. Furthermore, compared to magnetic saturation, the diagonal diffuse streaks which can be observed at $\Theta_i = \Theta_1$, as well as at $\Theta_i = \Theta_C$ (condition for Yoneda scattering), are considerably enhanced in the region close to the 1st order Bragg peak and close to the specular ridge. The theory of off-specular scattering from chemically or magnetically rough interfaces is still under development and without rigorous analysis it is impossible to obtain quantitative values of structural or magnetic attributes of the lateral inhomogeneities in this multilayer system. However, at least some qualitative statements can be made using the concept that a single-domain state would cause no magnetic diffuse scattering (magnetic saturation). With an increasing number of domains of decreasing size, the diffuse scattering extends further into the off-specular region. That is, for the present (Θ_i, Θ_f) map, recorded at a field close to the coercive field H_{CA}, enhanced diffuse scattering is observed mainly in a region close to the specular ridge, indicating that relatively large domains are present during this reversal process.

Comparing finally the intensity maps close to the coercive fields H_{CP} at $H = 112$ Oe and close to H_{CA} at $H = -599$ Oe in the 2nd hysteresis cycle with those obtained for magnetic saturation and for $H_{CA} \approx -883$ Oe in the first cycle, the specularly reflected intensity is strongly reduced and there is a large amount of diffuse scattering nearly evenly distributed in the small angle region. The diffuse intensity scattered from magnetic inhomogeneities is superimposed onto the streaks appearing at $\Theta_i = \Theta_C$ and $\Theta_i = \Theta_1$, which are still observable. Compared to the intensity map recorded at $H_{CA} = -883$ Oe, the diffuse scattering extends further into the off-specular region, suggesting that there is an increased distribution of lateral magnetic domains of smaller

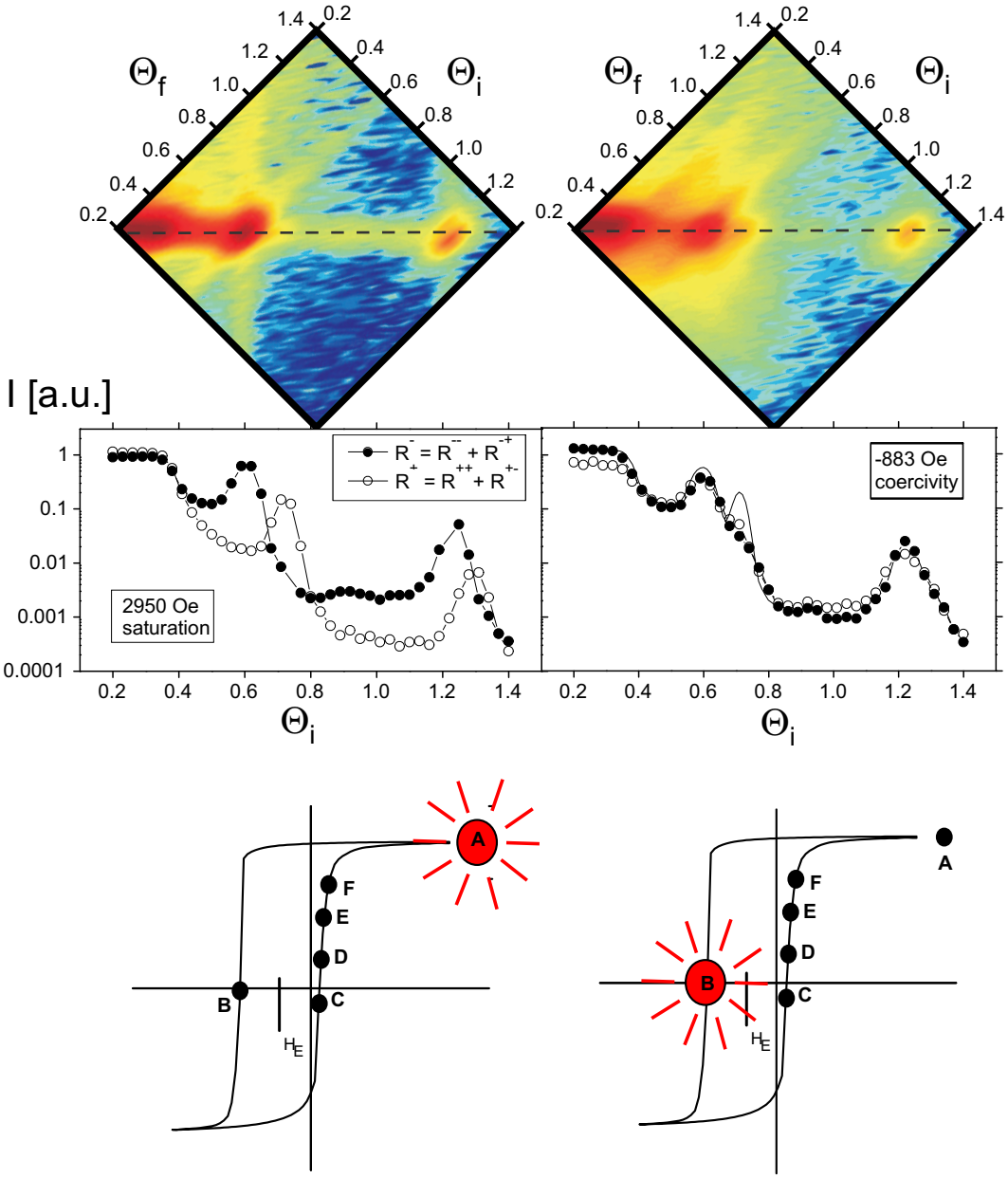

Figure 5.11: Top: (Θ_i, Θ_f) intensity maps for down-neutrons scattered from a $[Co/CoO/Au]_{20}$ multilayer in magnetic saturation (left) and at the coercive field H_{CA} (right). The spins of the incident neutrons are aligned along the applied field axis. Below each map the corresponding specular reflection profile is given for incoming up (open circles) and down (closed circles) neutrons. A fit curve (solid line) is added in the right-hand reflectivity profile simulating the presence of domains either parall (50 %) or antiparall (50 %) to the applied field. For comparison the magnetization curve of the multilayer in the biased state, measured by SQUID, is given at the bottom. A boldface circle marks the position in the hysteresis where the neutron data were recorded.

size. This experimental finding is consistent with the corresponding specular PNR experiment, where a significant intensity loss was observed at small incident angles (up to the 1st order Bragg peak) together with a broadening of the multilayer Bragg peak.

In summary, the off-specular scattering experiments performed with polarized neutrons give useful additional information about the nature of the magnetization reversal processes. While the specular PNR measurements are sensitive to magnetization rotation, the off-specular scattering gives information about vertical correlations and about lateral magnetic domain distributions. Without rigorous analysis it is impossible to obtain quantitative values describing structural and magnetic attributes of the lateral inhomogeneities. However, as a first approach, some qualitative statements can be extracted from the off-specular scattering results giving information in addition to the results obtained from specular PNR experiments with spin analysis: from the specular scattering experiment it is known that the magnetization reversal at H_{CA} is dominated by growth of domains which are directed either parallel or antiparallel to the applied field, while the off-specular PNR measurement reveals that these domains are relatively large. The magnetization reversal processes at the coercive fields H_{CP} and H_{CA} (2nd cycle), as measured by specular PNR, were characterized by magnetization rotation, while the intensity was considerably reduced compared to magnetic saturation and the multilayer Bragg peak was somewhat broadened. The off-specular scattering experiments could confirm the assumption that the missing intensity, which is re-distributed into the off-specular scattering region, arises due to scattering from a distribution of smaller lateral domains of different size.

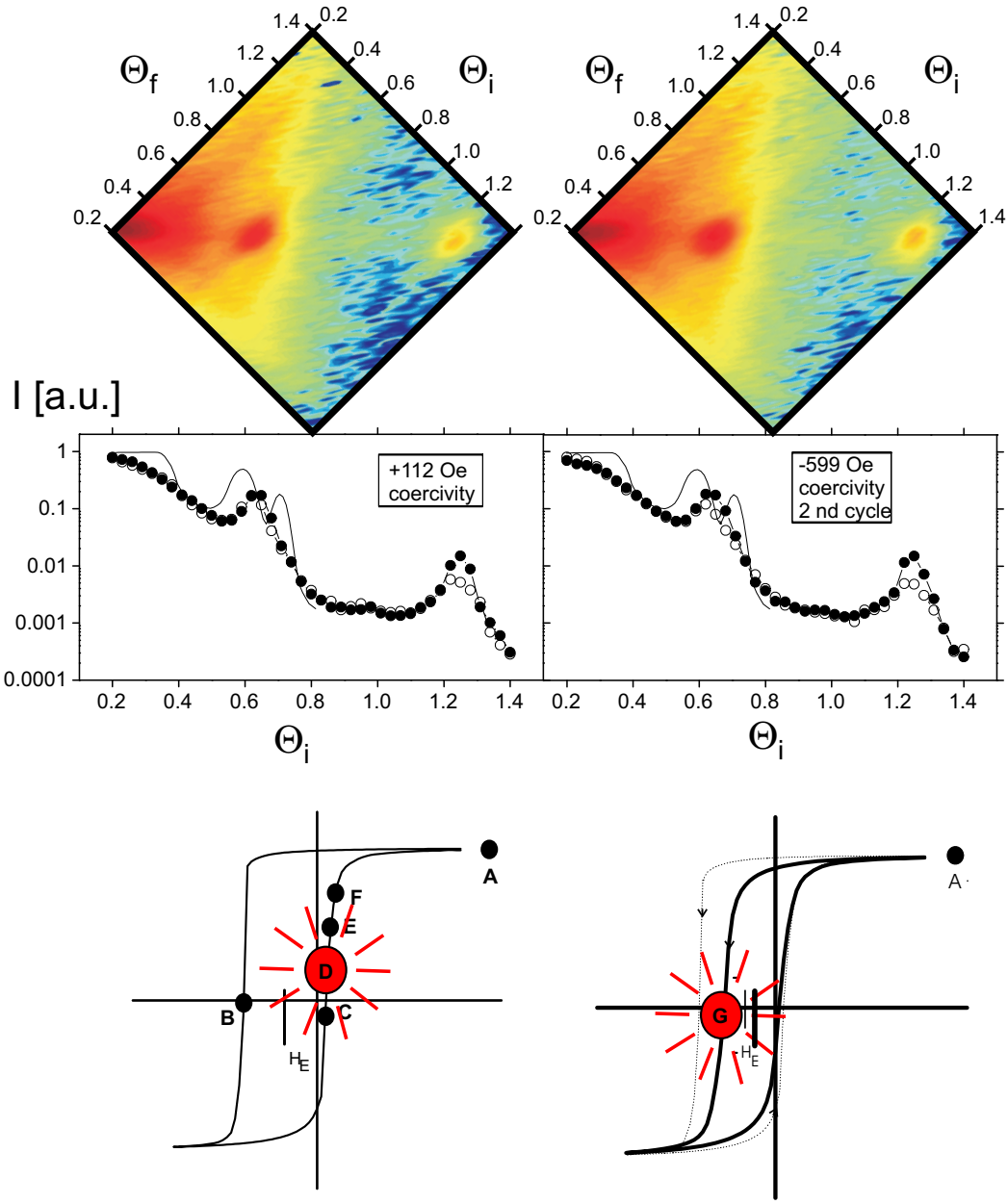

Figure 5.12: Top: (Θ_i, Θ_f) intensity maps for down-neutrons scattered from a $[\mathrm{Co/CoO/Au}]_{20}$ multilayer at the coercive field H_{CP} of the first cycle (left) and at the coercive field H_{CA} of the 2nd (= training) cycle (right). Below each map, the corresponding specular reflection profile is given for incoming up (open circles) and down (closed circles) neutrons. The fit curves (solid lines) added to the specular reflectivity profiles simulate the presence of domains either parall (50 %) or antiparall (50 %) to the applied field. In contrast to the reversal process at H_{CA} of the 1st cycle, these curves obviously do not describe the domain distributions at these fields. For comparison, the magnetization curve of the multilayer in the biased state, measured by SQUID, is given at the bottom. A boldface circle marks the position in the hysteresis where the neutron data were recorded.

5.4 Conclusion and summary of the PNR results

The origin of the asymmetric magnetization reversal processes on opposite sides of the same hysteresis loop is most likely connected with the strongly unidirectional character of EB coupling for the present multilayer. For this $[Co/CoO/Au]_{20}$ multilayer an appreciable energy barrier for reversal may be present only opposite to the bias direction, probably due to formation of domain walls in the AFM [Nik98, Nik00, MSBK87, Mal87, SM99a, Ges00]. Recent investigations have shown that depending on the particular system domain wall motion and rotation can both play a major role for the reversal [Nik98, Nik00, FYL$^+$00, PPLdM$^+$00, LFY$^+$01, BK71, CYC$^+$00]. In some cases soft magnetic NiFe alloys were used as FM material and FeMn alloys as AFM material, and domain wall motion was observed on both sides of the hysteresis loop [Nik98, Nik00, BK71]. In another experiment, a wedge-shaped NiFe/FeMn bilayer was probed, and an asymmetry of the domain wall motion for increasing and decreasing fields was found. This has also been attributed to the formation of domain walls in the AFM [Nik00].

The situation is more complicated for complex microstructures of the AFM such as in MnF_2/Fe and FeF_2/Fe bilayers investigated by Fitzsimmons *et al.* [FYL$^+$00, LFY$^+$01]. In this case an asymmetry in the reversal has been observed only for a certain cooling field orientation: rotation for decreasing fields and domain wall motion for increasing fields. The observed orientation dependence with respect to the cooling field and the type of reversal have been explained by an effective "45° coupling" which is caused by the twinned nature of the AFM studied. In this case the tendency of the unidirectional anisotropy to align the magnetization with the bias direction has been assumed to favor domain wall motion rather than rotation only for increasing fields. As opposed to this result, the dominant reversal mechanism on the increasing field branch for the present $[Co/CoO/Au]_{20}$ multilayer system is definitely magnetization rotation.

The reason for this difference is most likely due to different properties of the AFM materials used. While the AFM structures of MnF_2 and FeF_2 exhibit a magnetocrystalline anisotropy with a well defined anisotropy axis, the intrinsic anisotropy directions present in the granular CoO film are possibly averaged out over a large number of grains. Therefore in the EB state of the present multilayer there is mainly one prominent direction, which is the direction of the induced exchange bias. For other AFM structures, such as MnF_2 and FeF_2, in addition to the EB direction, other different prominent directions are present. These prominent directions certainly affect the magnetization reversal

process in different ways and it is difficult to separate the effects caused by different magnetic anisotropies. More importantly, since there is no other (intrinsic) prominent direction, the strength of EB and the type of reversal do not significantly depend on the cooling field orientation in the case of the present CoO layers.

Furthermore, the extremely different film thicknesses of 50 nm for MnF_2 and of only 2 nm for CoO may strongly influence domain wall formation in the AFM. It should be noted that reversal asymmetry for MnF_2/Fe has been found for a cooling field orientation corresponding to a relatively weak EB effect ($H_E = -30$ Oe, $E_{INT} \approx$ 0.06 erg/cm^2 and $H_E/H_C = 0.20$) as opposed to the strong EB effect in the present system ($H_E = -393$ Oe, $E_{INT} \approx$ 0.9 erg/cm^2 and $H_E/H_C = 0.78$). The strong EB in the present system might be attributed to a larger number of uncompensated spins at the AFM interface which are present in this type of thin granular AFM film. The uncompensated spins might act as pinning centers for domain walls in the ferromagnet [GR00a].

It can be assumed that the vertically correlated waviness of the present multilayer, as revealed by TEM imaging, may additionally affect the formation of domains in the Co layer during the reversal processes. In the present case, specular PNR measurements revealed that the reversal process on the decreasing field branch (opposite to the cooling field direction) is dominated by the formation of domains aligned either parallel or antiparallel to the applied field, while off-specular scattering experiments indicate that rather large domains are present. In contrast the reversal on the increasing field branch (parallel to the cooling field direction) is characterized by magnetization rotation, as measured by specular PNR with spin analysis, while off-specular scattering experiments revealed the presence of an increased distribution of domains of different size during this reversal process. In the 2nd (= training) cycle of the hysteresis, the magnetization reversal at the decreasing field branch is similar to the reversal at the increasing field branch. In this case it becomes clearly energetically favorable for the magnetization to break up into domains of different size with a more isotropic distribution of in-plane magnetization vectors.

The present results emphasize the necessity to clearly distinguish between different groups of systems both experimentally and theoretically even if asymmetric reversal processes occur in many different EB systems. The present multilayer is one example of a type of EB system consisting of granular FM and particularly thin granular AFM layers where the direction of induced EB in the biased state is the only prominent direction.